41st AIAA Fluid Dynamics Conference and Exhibit
27 - 30 June 2011, Honolulu, Hawaii

AIAA 2011-3873

Spanwise Growth of the Turbulent Spot Pressure-Fluctuation Field in a Hypersonic Boundary Layer

Katya M. Casper*

School of Aeronautics and Astronautics, Purdue University, West Lafayette, IN 47907-1282

Sandia National Laboratories, Albuquerque, NM 87185

Steven J. Beresh†

Sandia National Laboratories, Albuquerque, NM 87185

Steven P. Schneider‡

School of Aeronautics and Astronautics, Purdue University, West Lafayette, IN 47907-1282

The pressure-fluctuation field beneath wave packets and turbulent spots in a hypersonic boundary layer was studied on the nozzle wall of the Boeing/AFOSR Mach-6 Quiet Tunnel. For a controlled study, the breakdown of disturbances created by spark perturbations was measured at various freestream conditions. A disturbance first grows into a linear instability wave packet and then quickly becomes nonlinear. At this point, the wave packet is still concentrated near the disturbance centerline, but weaker disturbances are seen spreading from the center. Breakdown to turbulence begins in the core of the wave packets where the wave amplitudes are largest. Second-mode waves are still evident in front of and behind the breakdown point and can be seen propagating in the spanwise direction at a spreading angle. The turbulent core grows downstream resulting in a turbulent spot with a typical arrowhead shape. However, the spot is not merely a localized patch of turbulence; instability waves are still an integral part of the disturbance.

Nomenclature

Φ	power spectral density $((p'/p_\infty)^2/Hz)$	U_∞	freestream velocity (m/s)
f	frequency (kHz)	y	tunnel spanwise coordinate measured from the centerline of the spark perturber along the circumference of the wall, positive to the right looking upstream (m)
M	freestream Mach number		
p'	pressure fluctuation, $p - p_\infty$ (Pa)		
p_∞	freestream static pressure (Pa)		
P_0	tunnel stagnation pressure (kPa)	z	tunnel axial coordinate measured from throat (m)
Re	freestream unit Reynolds number (1/m)		
T_0	tunnel stagnation temperature (K)		

I. Introduction

Hypersonic reentry vehicles are subjected to high levels of fluctuating pressures. These intense fluctuations can cause vibration of internal components and lead to structural problems. There is a need to

*Research Assistant and Sandia Graduate Intern, Student Member AIAA, kcasper@purdue.edu, (765) 494-3348
†Principal Member of the Technical Staff, Engineering Sciences Center, Associate Fellow AIAA
‡Professor, Associate Fellow AIAA

Sandia National Laboratories is a multi-program laboratory managed and operated by Sandia Corporation, a wholly owned subsidiary of Lockheed Martin Corporation, for the U.S. Department of Energy's National Nuclear Security Administration under contract DE-AC04-94AL85000.

predict the magnitude, location, and spatial extent of the pressure fluctuations to better design hypersonic flight vehicles. Current designs often use overly conservative estimates of the fluctuations that can lead to heavier vehicles and degraded flight performance. Some correlations exist for the magnitude of transitional and turbulent pressure fluctuations, but these were derived primarily using either incompressible data or conventional (noisy flow) hypersonic wind-tunnel tests.[1] Such modeling efforts have not led to sufficient physical understanding of the transitional pressure fluctuations or adequate predictive capabilities.

Wind-tunnel tests at fixed freestream conditions have shown that transitional pressure fluctuations can be more severe than turbulent pressure fluctuations,[2–6] making transitional fluctuations of primary interest for this work. The transition process can be described through intermittency and the growth and propagation of turbulent spots in the transitional boundary layer.[7] These turbulent spots create wall pressure fluctuations. By combining the pressure fluctuations associated with wave packets and turbulent spots into a model of transition, the models can be extended to calculate transitional pressure fluctuations from fundamental physics. This type of model has already been developed for incompressible flow on a flat plate.[8] Recent direct numerical simulation (DNS) efforts have computed the pressure field for wave packets and developing turbulent spots in hypersonic boundary layers.[9–12] Recent experimental measurements have also begun to measure the internal structure of spots in pressure data under a hypersonic boundary layer.[13]

Turbulent spot pressure fluctuations were measured on the nozzle wall of the Boeing/AFOSR Mach-6 Quiet Tunnel (BAM6QT). The BAM6QT can be operated under quiet flow conditions. Under quiet flow, laminar boundary layers are maintained on the wall of the wind tunnel. Laminar flow avoids the generation of acoustic "noise" usually radiated from the turbulent boundary layers on the walls of conventional tunnels. Because the boundary layer grows over the entire nozzle length, it is on the order of ten millimeters thick in the test section. As a result, the second-mode instability waves occur at low frequencies. Also, turbulent spots can grow large along the nozzle length. The smaller spots can be many centimeters long, with the largest spots on the order of a meter long. These spots allow sufficient frequency and spatial resolution with available pressure instrumentation. Naturally-occurring disturbances on the tunnel wall can be observed. However, they cannot be repeated and their spanwise location relative to the sensors is unknown. In order to study controlled disturbances, a spark perturber is used to create large repeatable disturbances. Instability wave packets as well as their development into turbulent spots can then be measured. A study of the disturbance centerline was reported in Ref. 13. The present paper extends that work to study spanwise measurements at similar freestream conditions. By studying controlled disturbances and their breakdown into turbulent spots, a better understanding of the transitional physics can be gained. This increased understanding of the pressure fluctuations associated with transition can then be included in engineering models for predicting a flight vehicle's environment.

II. Experimental Setup

A. Boeing/AFOSR Mach-6 Quiet Tunnel

Measurements were made on the nozzle wall of the Boeing/AFOSR Mach-6 Quiet Tunnel (Fig. 1). This tunnel is one of two hypersonic quiet tunnels in the world. Because it can be operated as a conventional noisy tunnel or as a quiet tunnel, freestream noise effects can be studied. The tunnel is a Ludwieg tube – a long pressurized tube with a converging-diverging nozzle on the end. The flow passes from the driver tube, through the test section, diffuser, and finally to the vacuum tank. Flow is initiated by bursting a double diaphragm that is located downstream of the diffuser. When the flow begins, an expansion wave travels upstream and then reflects between the upstream end of the driver tube and the contraction. The total pressure and temperature drop with each reflection cycle (every 200 ms) until the tunnel unstarts. Run times of 3–5 s under quiet flow conditions are typical at present. The tunnel uses air as the test gas and operates with an initial total pressure P_0 of 34–2070 kPa and an initial total temperature T_0 of 430 K. These conditions give a freestream unit Reynolds number range of $0.4–18.3 \times 10^6/m$, calculated using Keyes's law for viscosity.[14] The current maximum quiet stagnation pressure is 1170 kPa. The test-section diameter is 0.242 m at the nozzle exit, and the nozzle is 2.590 m long. Noise levels vary from 2–4.5% under noisy flow conditions. Under quiet flow conditions, noise levels are 0.05% or less.[15]

Obtaining such quiet flow in a hypersonic tunnel is not a trivial task. The nozzle is polished to a mirror finish to avoid roughness-induced transition, and the contraction boundary layer is also removed by bleed slots at the throat. A new laminar boundary layer then begins just upstream of the nozzle throat and is maintained through the test section. In addition, the air is filtered to remove dust or other particles above

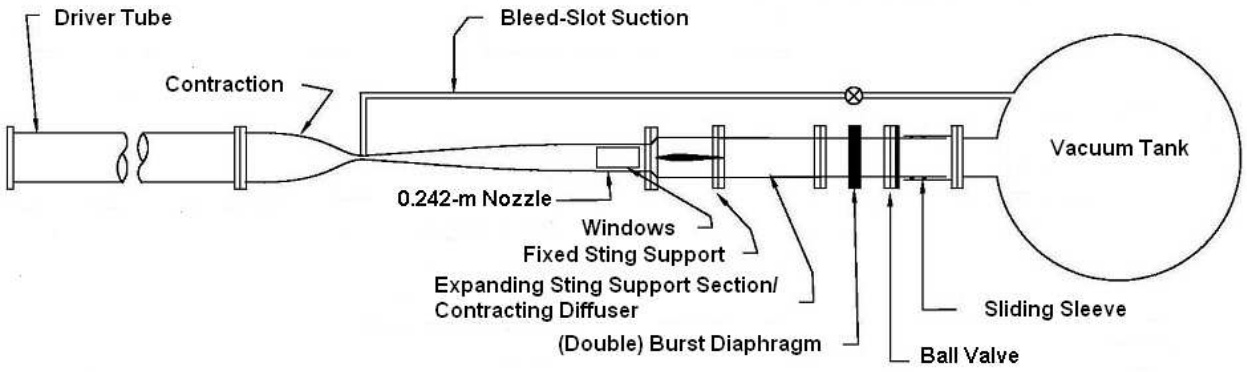

Figure 1. Boeing/AFOSR Mach-6 Quiet Tunnel

0.01 microns that may damage the nozzle or trip the boundary layer. More details about the development of the BAM6QT can be found in Schneider.[16]

B. Controlled Generation of Wave Packets and Turbulent Spots using Spark Perturbations

In order to create large flow disturbances that lead to formation of instability wave packets and turbulent spots within the length of the test section, a high-voltage spark perturber is used. The spark perturber creates a rapid, broadband frequency impulse capable of generating an instability wave packet. The spark perturber uses an electrode design that isolates the ground from the tunnel, reducing electrical noise during spark generation. This design has two 1.1-mm diameter stainless steel electrodes in a Macor mount. The spacing between electrodes is 1.3 mm. The perturber uses an ignition coil and timing circuit to create sparks across the electrode. The ignition coil always remains charged until a spark is desired. When the coil is suddenly shut off, a spark is created. The spark is typically pulsed at 200 Hz to allow measurements of the resulting disturbances in the intervals between the RF noise generated by the spark. The perturbation is turned off while disturbances generated by the spark convect downstream over the sensors.

C. Instrumentation and Data Acquisition

Kulite XCQ-062-15A pressure transducers are used to measure surface pressure fluctuations. These transducers use silicon diaphragms as the basic sensing mechanisms. Each diaphragm contains a fully active four-arm Wheatstone bridge. The sensors are mechanically stopped above 103 kPa to prevent damage to the diaphragms at the high BAM6QT pre-run pressures. They have a resonant frequency between 250–300 kHz. The repeatability of the sensors is approximately 0.1% of the full scale, or 0.1 kPa. The Kulites have screens to protect the diaphragms from damage. For these tests, only A-screen sensors were used. The A-screen has a large central hole. This screen offers only a small amount of diaphragm protection, but the sensor has a flatter frequency response up to 30–40% of the resonant frequency.[17] The sensitive area of the A-screen sensor is the hole size (0.81 mm^2). The Kulites are only used to obtain the AC signal. The sensors have a repeatable, linear calibration slope which can be used to determine the fluctuating component of the signal (within the flat dynamic range of the sensor).[18] The fluctuations were normalized by the freestream pressure, computed using the total pressure and freestream Mach number in the tunnel.

The signal from the Kulite pressure transducers was processed by custom-built electronics, which also supply a 10 V excitation. The output signal was amplified by a gain of 100 with an INA103 instrumentation amplifier chip to give the DC signal. Tektronix TDS7104, DPO7104, two TDS5034B, and two DPO7054 Digital Phosphor Oscilloscopes were used for data acquisition. The scopes have an 8-bit vertical resolution, but the resolution can be increased to over 11 bits in Hi-Res mode. Hi-Res mode is also used to provide digital filtering. The oscilloscopes average in real time at the maximum sampling rate of 1.25–5 GS/s (depending on the model) for 4 input channels and then save data at the specified sampling rate. The data sampling rate for these measurements was 500 kHz. Pressure traces were post-processed by low-pass filtering the data at

150 kHz using an 8-pole digital Butterworth filter (48 dB of attenuation per octave). This filtering removes sensor diaphragm resonance from the pressure traces to show the underlying data more clearly.

D. Setup

A schematic of the experimental setup is shown in Fig. 2. There is a slot in the top wall of the tunnel near the nozzle exit to allow traverse measurements with a Pitot probe or a hot wire. A plug was fabricated to fill this slot. Kulites were placed at four locations on the plug centerline (z = 2.201, 2.302, 2.378, and 2.480 m, where z is the axial tunnel coordinate measured from the throat). The spark perturber is placed at z = 1.924 m, upstream of this plug in another insert on the top wall of the tunnel. These locations are marked on the axis at the top of Fig. 2 and are shown in Fig. 3(a).

Initial measurements showed that spark-induced wave packets had only begun to break down near the nozzle exit, even at the maximum quiet *Re* in the BAM6QT. Additional tunnel hardware was constructed to allow measurements downstream of the nozzle exit. Previous measurements have shown that the nozzle wall boundary layer appears laminar well downstream of the nozzle exit.[15,19] In order to take advantage of this additional length of laminar flow, a cylindrical pipe insert was designed that fits between the nozzle exit and the diffuser sting support as visible in Fig. 2. This insert has the same diameter of 0.242 m as the nozzle exit. When the tunnel is closed, the pipe insert fits flush with the nozzle exit and extends 0.254 m downstream. Fig. 3(b) shows the pipe insert installed in the BAM6QT. At the downstream end of the pipe insert, there is a step at the beginning of a nylon diffuser section that was created when the nylon section curled inward during machining. The effect of this step on the data is discussed in more detail later. A new stainless-steel downstream section has already been constructed that eliminates this step for future tests. For centerline measurements, Kulites were located at z = 2.628, 2.679, 2.730, 2.781, and 2.831 m on the top wall of the pipe insert. These sensor locations are visible in the photograph in Fig. 3(b) and are marked on the axis in Fig. 2.

The pipe insert is actually made of five rings as shown in Fig. 4(a). One of the downstream rings has azimuthal sensor locations at ± 5, 10, 15, 20, and 30 degrees from the top wall of the tunnel (Fig. 4(b)). These locations correspond to y = ± 11, 21, 32, 42, and 63 mm, where y is measured from the centerline of the spark perturber position along the circumference of the wall. The four downstream rings are interchangeable to allow azimuthal measurements at any of the four downstream locations enumerated in the previous paragraph.

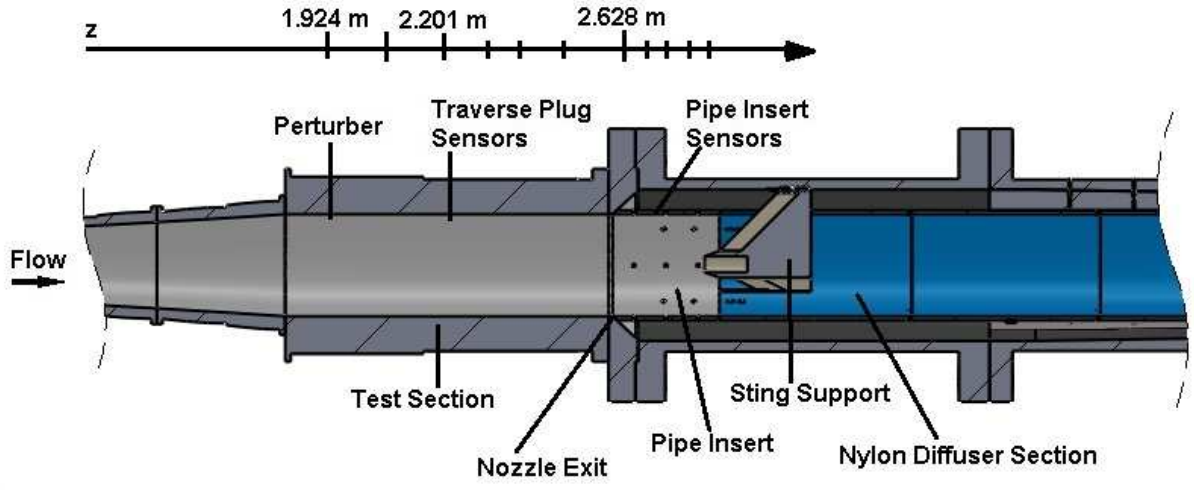

Figure 2. Schematic of experimental setup in the BAM6QT for nozzle-wall measurements. Perturber and sensor locations are marked on the z axis.

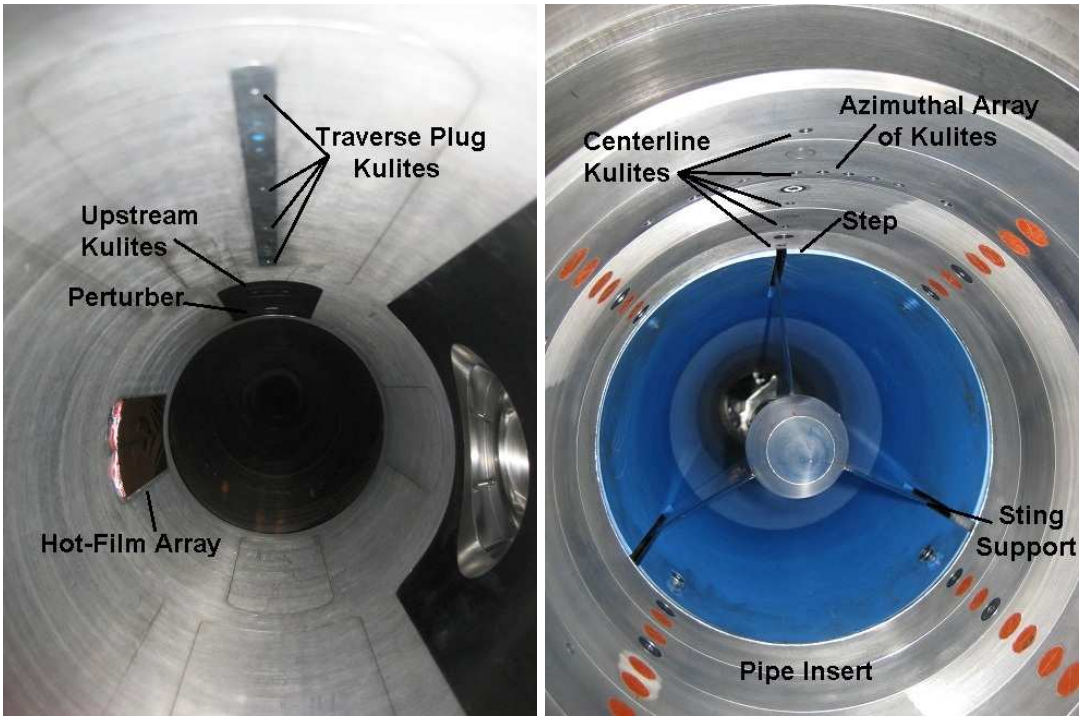

(a) (b)

Figure 3. Experimental setup in the BAM6QT; (a) Looking upstream; (b) Looking downstream.

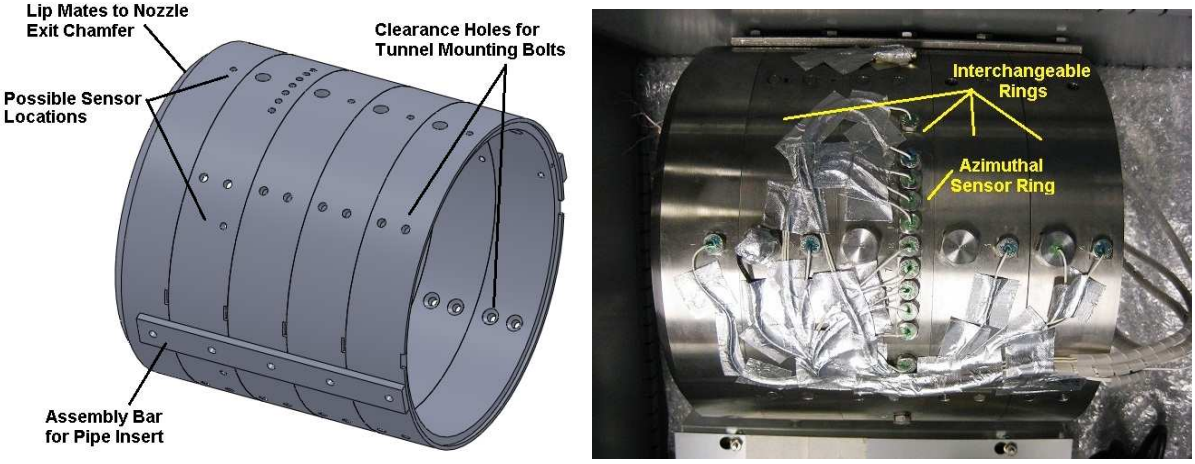

(a) (b)

Figure 4. Multi-ring pipe insert (external view); (a) CAD model; (b) Hardware with sensors installed.

III. Experimental Results

Spanwise measurements of the spark-induced disturbances were made at varying Re from $5.76 - 10.8 \times 10^6/m$ and at varying downstream locations between z = 2.679 and 2.831 m. These measurements were made at similar freestream conditions to the centerline measurements in Casper et al.[13] Because the spark perturbations are generated at 200 Hz, multiple disturbances can be averaged. The averaging trigger was the 200-Hz square-wave input signal to the perturber. Ensemble-averaged pressure traces of a 3-ms time period after the spark were computed for 50 disturbances. These traces were chosen from a 0.5-s interval of a run, after the perturber had been running for a few tenths of a second. More repeatable results are obtained after the perturber has warmed up. Also, even though Re drops within this 0.5-s interval, the change is smaller than 4% and no noticeable effects are seen in the results. Any disturbances that were contaminated by naturally-occurring turbulent spots or smaller disturbances were not used in the averages. These natural disturbances occurred infrequently and were identified using an RMS threshold criteria on the laminar boundary-layer data measured by a single sensor between spark-induced disturbances. An upstream nozzle-wall sensor was used for this criteria since spark-induced disturbances are still small within the nozzle and the majority of the measured pressure traces contain undisturbed laminar boundary layer data. Large natural disturbances that occasionally occurred simultaneously with the spark-induced disturbance were also identified and removed by a different threshold criteria.

An ensemble-averaged power spectral density (PSD) was also computed by averaging together the fast-Fourier transform (FFT) of each of the 3-ms pressure traces and normalizing to obtain the power spectral density. This ensemble-averaged power-spectral density is not the same as taking a PSD of the ensemble-averaged pressure traces. This difference is most apparent when wave packets began to break down. Even though the packets show good repeatability while growing, their breakdown varies from packet to packet, and the pressure fluctuations are no longer in phase. As a result, the ensemble-averaged pressure traces smooth out the turbulent fluctuations seen during breakdown. Since phase information is not contained in the FFT, ensemble averaging FFT's does not remove the large fluctuations during breakdown but instead creates an average representation of the frequency content of the individual samples.

Results at lower freestream Re show the development of small linear wave packets into large nonlinear packets. Fig. 5 shows ensemble-averaged centerline measurements at a low Re of $6.33 \times 10^6/m$. Pressure traces are vertically offset proportional to z. The PSD shows only every tenth point for clarity. At this Re, an instability wave packet develops over the nozzle wall sensors. The peak frequency of the waves can be seen in the PSD as it decreases from 36 kHz to 21 kHz farther downstream. This instability is the second mode which acts like a trapped acoustic wave in the boundary layer. As a result, the frequency of the second-mode waves is proportional to approximately twice the boundary layer thickness. As the boundary layer thickens downstream, the frequency of the second-mode waves decreases. The frequency of the nozzle-wall instability waves has been shown to be in good agreement with computations of second-mode waves on the nozzle wall.[13] Through z = 2.628 m, the wave packet is small and appears linear, as evidenced by the lack of any harmonics in the PSD. Farther downstream, the wave packet becomes nonlinear as indicated by the presence of harmonics in the PSD. For example, at z = 2.679 m, there is a single harmonic in the spectra at 60 kHz. At z = 2.781 m, second and third harmonics are visible at 44 and 66 kHz, respectively. Once the nonlinear waves become large enough, other peaks appear in the spectra above and below the fundamental frequency and its harmonics. For example, additional peaks at z = 2.781 m are visible at 7, 16, 29, 34, and 51 kHz, among others. The origin of these additional peaks is unclear.

The centerline behavior of the wave packet is supplemented by spanwise measurements. Fig. 6 shows contour plots of the spanwise pressure fluctuation measurements at the four most downstream sensor locations. Spanwise measurements are shown as a function of y. Time traces of the pressure fluctuations were converted to an approximate z coordinate using an average convection velocity of the disturbances. The middle of the time traces (t = 1.5 ms) was set to correspond to each axial measurement location. When the time traces are converted to distance, a smaller time corresponds to a greater z location. As a results the front or leading edge of the disturbances corresponds to smaller t and larger z while the rear or trailing edge of the spot corresponds to larger t and smaller z. References to 'upstream' and 'downstream' still correspond to the freestream flow direction in the tunnel.

Two traces from z = 2.480 and 2.679 m were cross-correlated for each run in order to find an average disturbance convection velocity. Results from all runs were averaged to give a convection velocity of $0.8U_\infty$. This result is an approximation since the leading and trailing edges of the spot convect at different velocities and the disturbance is changing as it convects downstream. However, it allows an approximate comparison

of the spanwise and streamwise growth of the spots. The color scale of the contour plots is kept constant for all measurements at a single Re. The zero pressure contour lines were removed and replaced by minimum contour lines at $\pm$ 0.05 p'/p_∞ in order to compare the spanwise extent of the disturbances between varying Re. Other contour lines are displayed at intervals of 0.1 p'/p_∞. The overall scale of the plots is changed at other freestream conditions to better show the details of the disturbance structure.

At z = 2.679 m, the wave packet is clearly seen as alternating lines of positive and negative pressure fluctuations. However, the fluctuations tend to have a greater positive magnitude than negative, especially as they grow larger. These fluctuations are concentrated near the center of the disturbance and occur in a periodic and organized fashion. There are also weak disturbances spreading in the spanwise direction. At this point, the wave packet already shows nonlinearity along the centerline as indicated by the presence of a second harmonic in the spectra. Farther downstream, the large fluctuations of the wave packet are still concentrated near the centerline; however, the packet is becoming distorted. The wave packet fluctuations have started to bend along the spanwise propagation lines, and weaker disturbances are seen spreading in the spanwise direction. The centerline spectra in Fig. 5(b) at the downstream locations show multiple nonlinear harmonics as well as additional peaks in the spectra.

The time traces and PSD's of the spanwise measurements give additional insight into the wave-packet development (Fig. 7 through Fig. 10). The pressure traces are vertically offset proportional to y. The traces clearly show large second-mode waves on the centerline and their spreading in the spanwise direction. Small second-mode waves are still visible far from the centerline even at this low Re. At z = 2.679 m, two nonlinear harmonics are visible in the centerline spectra and also the first two off-center sensor locations. Farther away, small linear waves are seen at y = $\pm$ 32 mm. By y = $\pm$ 63 mm, smaller waves can be seen just above the electronic background noise. At z = 2.730 m, a similar result to that at z = 2.679 m is obtained; however, the amplitude of the waves has increased at all sensor locations. By the last two axial measurement locations, the spectra show additional peaks above and below the fundamental frequency and its harmonics. More broadband frequencies are beginning to be seen, but the spectra are still dominated by the second-mode waves. Away from the centerline, second-mode waves are clearly seen, with weak waves even extending beyond y = $\pm$ 63 mm. It is surprising that the second-mode waves extend far from the centerline even though the disturbance has not yet broken down to turbulence.

Some asymmetry is seen in the spark-induced disturbances. A smaller perturbation is measured at y = 11 mm compared to y = -11 m. This asymmetry is consistent with other measurements just downstream of the spark at z = 2.055 m (not shown). The disturbance near the perturber at z = 2.055 m seems to be centered about y = -1.2 mm, over one of the perturber electrodes. Similar asymmetry was seen at other Re as well. It is unknown whether this asymmetry is a result of the spark perturbation itself or of asymmetry in background disturbances in the tunnel. Small immeasurable non-uniformities in the freestream can impact results.[20] Also, for the tests at z = 2.730 and 2.781 m, the sensor at y = 42 mm measures significant levels of high-frequency electronic noise. This noise appeared for unknown reasons and could not be eliminated. However, the measurements at low frequency (below 40 kHz in these cases) are similar to the sensor at y = -42 mm. A similar result was obtained at other Re where electronic noise was again picked up by this sensor.

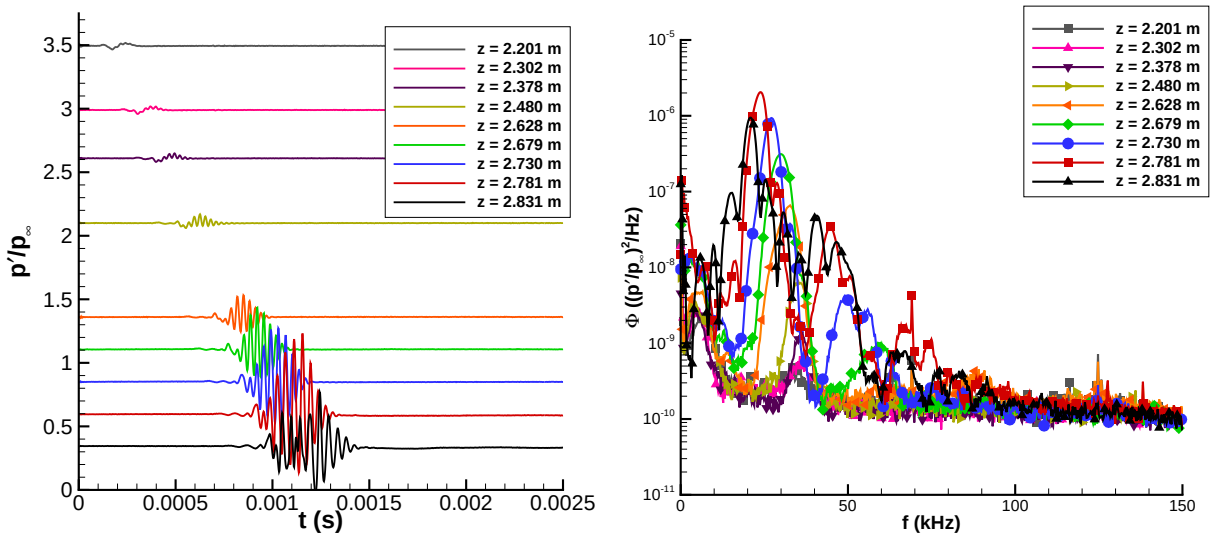

(a) (b)

Figure 5. Centerline measurements of ensemble-averaged disturbances, P_0 = 635.2 kPa, T_0 = 424.0 K, $Re = 6.33 \times 10^6/m$; (a) Pressure traces, each trace is vertically offset proportional to z; (b) Power spectral density.

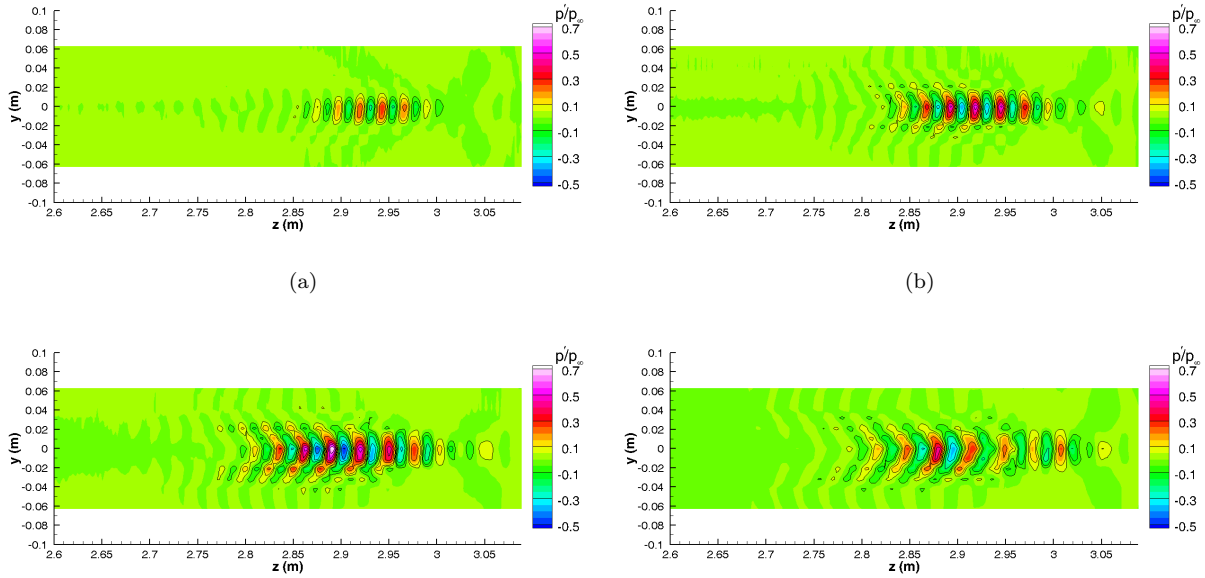

(a) (b)

(c) (d)

Figure 6. Contour plots of spanwise measurements of ensemble-averaged disturbances, P_0 = 627.9–640.1 kPa, T_0 = 423.9–424.0, $Re = 6.35 - 6.38 \times 10^6/m$; (a) z = 2.679 m; (b) z = 2.730 m; (c) z = 2.781 m; (d) z = 2.831 m.

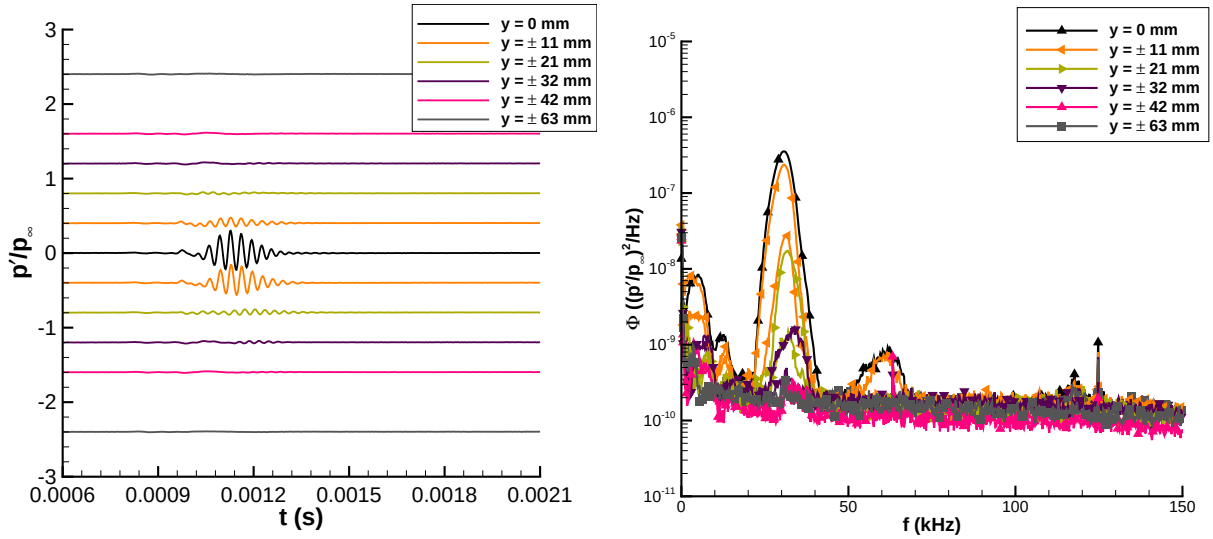

(a) (b)

Figure 7. Spanwise measurements of ensemble-averaged disturbances at z = 2.679 m, P_0 = 627.9 kPa, T_0 = 424.0 K, $Re = 6.36 \times 10^6/m$; (a) Pressure traces, each trace is vertically offset proportional to y; (b) Power spectral density.

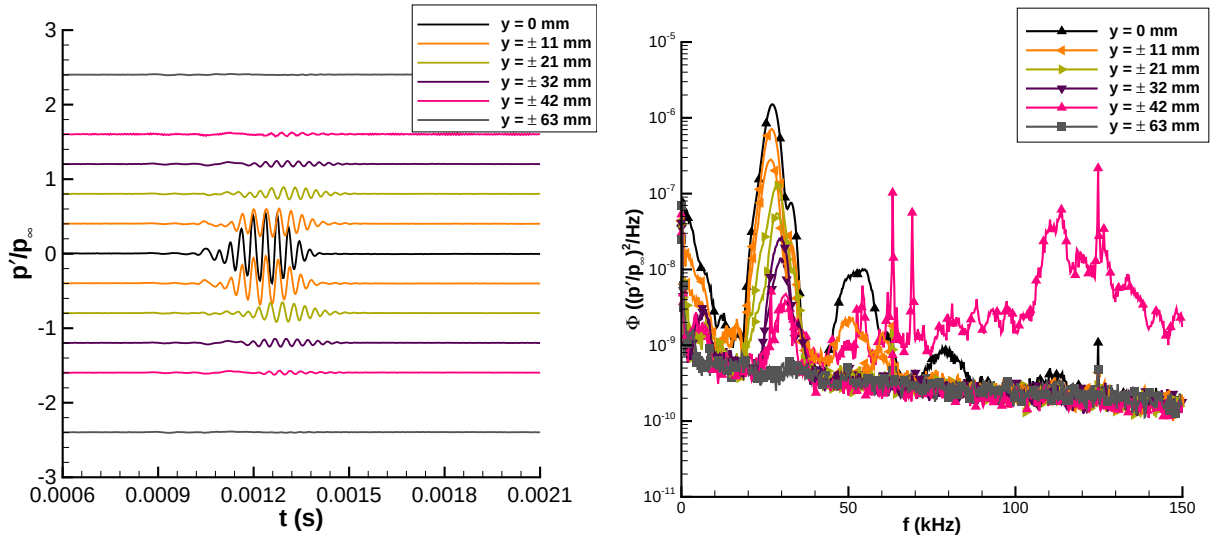

(a) (b)

Figure 8. Spanwise measurements of ensemble-averaged disturbances at z = 2.730 m, P_0 = 636.3 kPa, T_0 = 423.9 K, $Re = 6.35 \times 10^6/m$; (a) Pressure traces, each trace is vertically offset proportional to y; (b) Power spectral density.

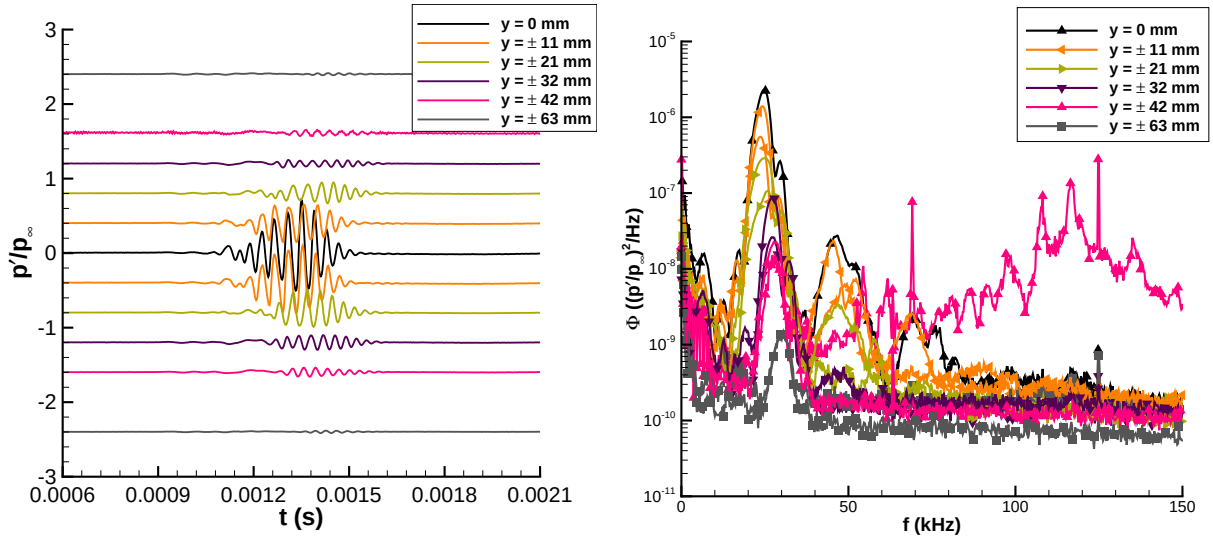

(a) (b)

Figure 9. Spanwise measurements of ensemble-averaged disturbances at z = 2.781 m, P_0 = 640.1 kPa, T_0 = 423.9 K, $Re = 6.38 \times 10^6/m$; (a) Pressure traces, each trace is vertically offset proportional to y; (b) Power spectral density.

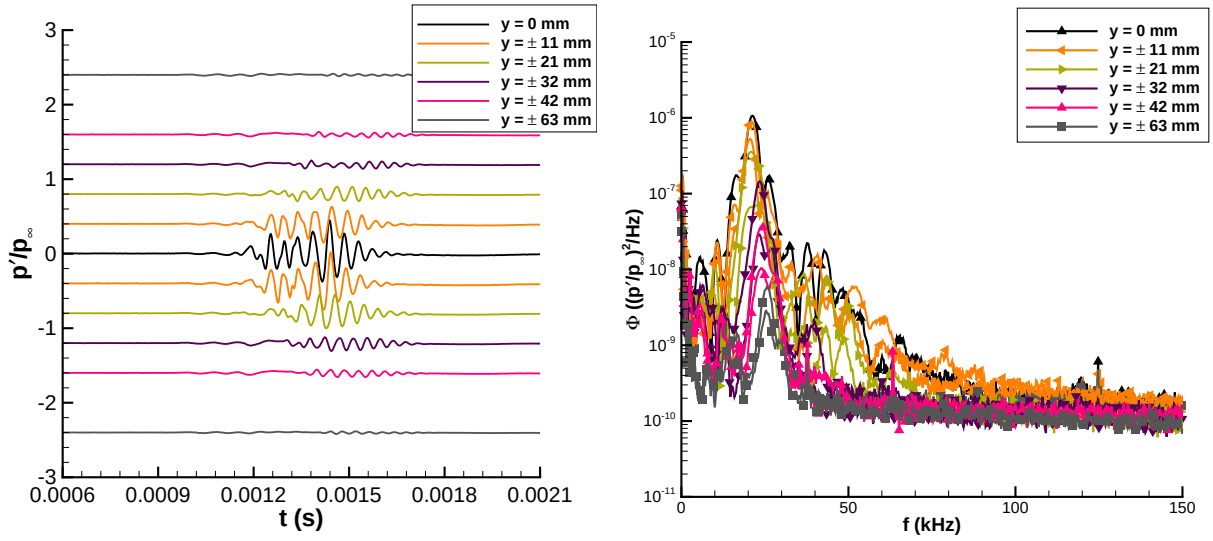

(a) (b)

Figure 10. Spanwise measurements of ensemble-averaged disturbances at z = 2.831 m, P_0 = 636.9 kPa, T_0 = 423.9 K, $Re = 6.35 \times 10^6/m$; (a) Pressure traces, each trace is vertically offset proportional to y; (b) Power spectral density.

At higher Re, a similar development of a second-mode wave packet is seen compared to the lower Re case. However, growth and breakdown of the waves happens farther upstream, allowing the continued breakdown of the waves and development of turbulent spots near the end of the measurement region where the spanwise sensors are located. Fig. 11 shows ensemble-averaged centerline measurements at an intermediate Re of $8.25 \times 10^6/m$. At this Re, a second-mode wave packet with frequencies between 33 and 43 kHz develops over the nozzle wall sensors. The frequency of the waves again decreases as the boundary-layer thickens downstream. The wave packet eventually becomes nonlinear as indicated by the presence of harmonics in the PSD beginning at z = 2.480 m where a harmonic is seen near 76 kHz. This is farther upstream than the lower Re condition where nonlinearity became apparent at z = 2.679 m. The waves then become very large with positive fluctuations greater than p_∞ before they break down near z = 2.730 m. It is surprising that such large fluctuations are seen before the waves break down. Negative fluctuations remain much smaller and do not approach zero absolute pressure. The spectra of these large wave packets show many peaks in the spectra along with elevated broadband frequencies.

Once breakdown occurs, the spectra show elevated broadband frequency components indicating the onset of turbulence in the boundary layer. Additional peaks in the spectra are no longer present. However, second-mode waves remain an integral part of the disturbance after breakdown. The waves are still seen at the front and rear of the disturbance. These residual waves appear as a broad peak in the spectra. At z = 2.831 m, a second pressure rise is seen behind the turbulent spot at t = 0.0015 s. It is believed that this is an upstream-traveling reflection of the spot's pressure fluctuations from the step in the tunnel 0.0254 m downstream of the sensor (Fig. 3(b)). This peak occurs only at the downstream end of the pipe insert and has been shown to be sensor independent. A new downstream section has been constructed to remove this step in future tests.

The pressure-fluctuation field within the disturbance as it breaks down into a turbulent spot is seen in contour plots at the four downstream measurement locations (Fig. 12). For the measurements at z = 2.679 m, the contour plot shows that the second-mode wave packet is still contained near the centerline. In the measurements farther downstream, the disturbance footprint still clearly shows the second-mode waves, but they have spread in the spanwise direction and become distorted. The spanwise edges of the wave packet are also jagged. By the measurements at z = 2.831 m, the spanwise spread of larger disturbances is evident and the characteristic arrowhead shape of the turbulent spots can be seen; however, it is unclear at which point the wave packet becomes a turbulent spot. There is a gradual change between the two cases. Breakdown of the waves occurs first on the centerline where the wave amplitudes are largest. However, traces of the second-mode waves can still be seen, especially at the front and rear of the disturbances as well as in the spanwise edges. Some criterion is needed to better define this transition point. A comparison of the spanwise width of the waves can be made to the coherence measurements by Kimmel et al.[21] They found that the spanwise coherence of second-mode waves was approximately four times the boundary layer thickness (approximately 9 mm thick at the nozzle exit in the present case). The width of the packets remains approximately within these bounds until z = 2.781 m when the waves begin to breakdown and stronger disturbances spread in the spanwise direction.

Time traces and PSD's of the spanwise measurements provide additional information about the disturbance structure. Results at the four downstream locations are shown in Fig. 13 through Fig. 16. As before, the sensor at y = 42 mm had an elevated electronic noise level when placed at z = 2.730 and 2.781 m. However, lower frequency measurements are again consistent with the sensor at y = -42 mm. At z = 2.679 m, the time traces show the wave-packet structure of the disturbance. The second-mode waves spread in the spanwise direction which results in a longer streamwise extent of the off-center waves at y = ± 11 mm compared to y = 0 mm. Farther from the center, the wave amplitudes decrease sharply, but small second-mode waves that are barely visible above the background electronic noise extend to y = ± 63 mm. The PSD of the traces show that the waves are large and nonlinear along the centerline. Farther from the centerline, the disturbances are much smaller and linear. No harmonics are seen in the spectra past y = ± 32 mm.

At z = 2.730 m, larger nonlinear waves are seen. Near the centerline, the disturbances show a rise in broadband frequency components and multiple peaks in the spectra. However, there are still only small disturbances measured away from the centerline. By z = 2.781 m, there are elevated broadband frequency components in the spectra near the centerline. At z = 2.831 m, the time traces again indicate turbulent fluctuations along the centerline. However, a peak at the second-mode frequency is still visible in the spectra. The second-mode waves are also visible in the time traces, especially near the front, rear, and edges of the spots. The PSD shows a gradual change from second-mode dominated spectra at the spot edges to more

broadband frequencies along the centerline.

Similar measurements were made at other Re between $5.76 - 10.8 \times 10^6/m$. As the Re increases, the second-mode waves grow in amplitude sooner and break down to turbulence farther upstream. The spanwise extent of the wave packets and spots increases with Re and spreads farther in the spanwise direction. Fig. 17 shows the centerline measurements from Casper et al.[13] near the maximum quiet Re in the tunnel. The waves break down into turbulent spots before they reach the downstream pipe-insert sensors, as indicated by broadband frequencies in the spectra. However as before, the exact location where a wave packet becomes a turbulent spot is still unclear as there is a gradual change between the two cases.

Fig. 18 shows contour plots of the pressure fluctuations at this high Re condition. The turbulent spot is large, even at z = 2.679 m. Farther downstream, the turbulent spot grows larger and spreads in the spanwise direction. Behind the spots, a negative pressure fluctuation region is seen. This corresponds to a 'calmed' region typically seen behind turbulent spots.[10] Some evidence of second-mode waves appears in this calmed region and is most clear in the measurements at z = 2.730 m. Second-mode waves also persist at the front and at the spanwise edges of the spot.

Time traces and PSD plots of the spanwise measurements at this Re are similar to the downstream measurements at $Re = 8.25 \times 10^6/m$ (Fig. 16). Results do not vary significantly with downstream distance. Fig. 19 shows typical results from measurements at z = 2.831 m. The character of the spot stays the same as it grows downstream. The turbulent core increases in size in the streamwise and spanwise directions but second-mode waves are still observed at the spanwise edges of the spot.

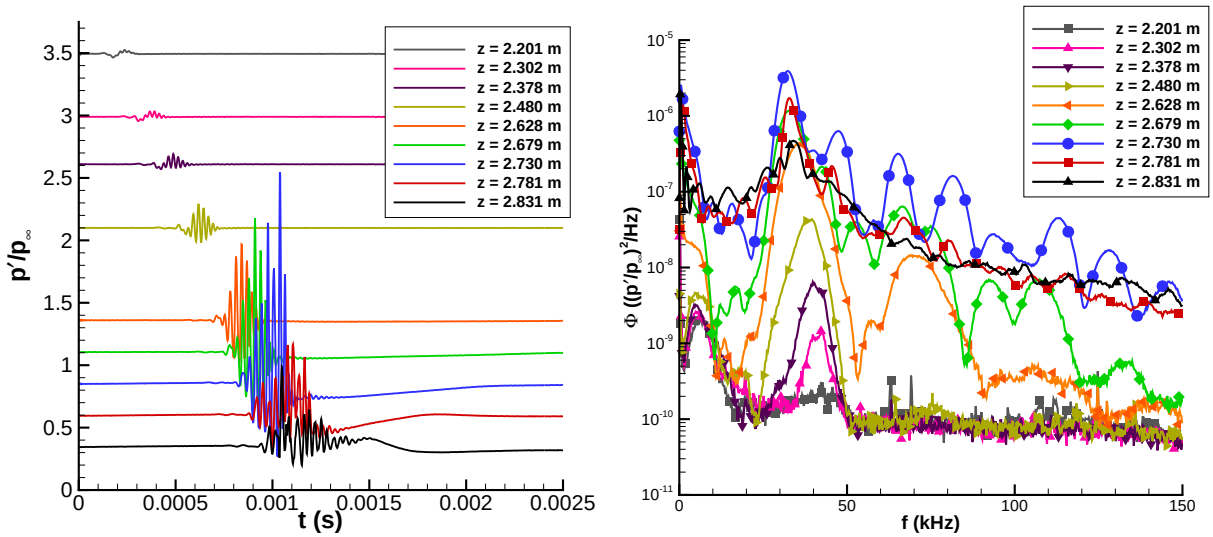

(a) (b)

Figure 11. Centerline measurements of ensemble-averaged disturbances, P_0 = 827.9 kPa, T_0 = 424.0 K, $Re = 8.25 \times 10^6/m$; (a) Pressure traces, each trace is vertically offset proportional to z; (b) Power spectral density.

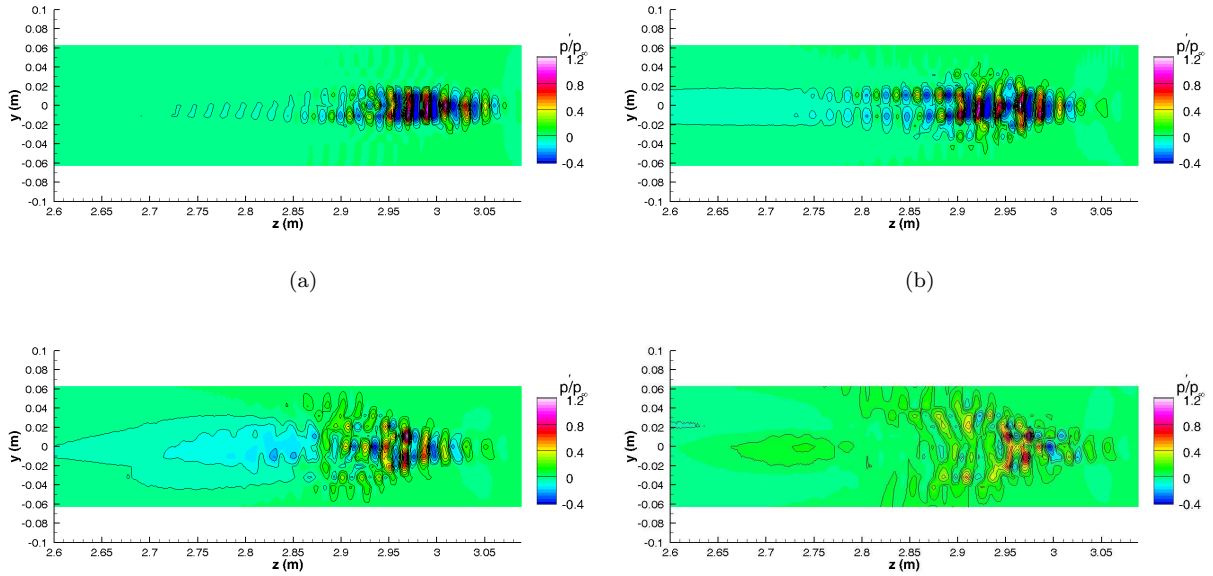

Figure 12. Contour plots of spanwise measurements of ensemble-averaged disturbances, P_0 = 834.3–839.5 kPa, T_0 = 423.8–423.9 K, $Re = 8.32 - 8.34 \times 10^6/m$; (a) z = 2.679 m; (b) z = 2.730 m; (c) z = 2.781 m; (d) z = 2.831 m.

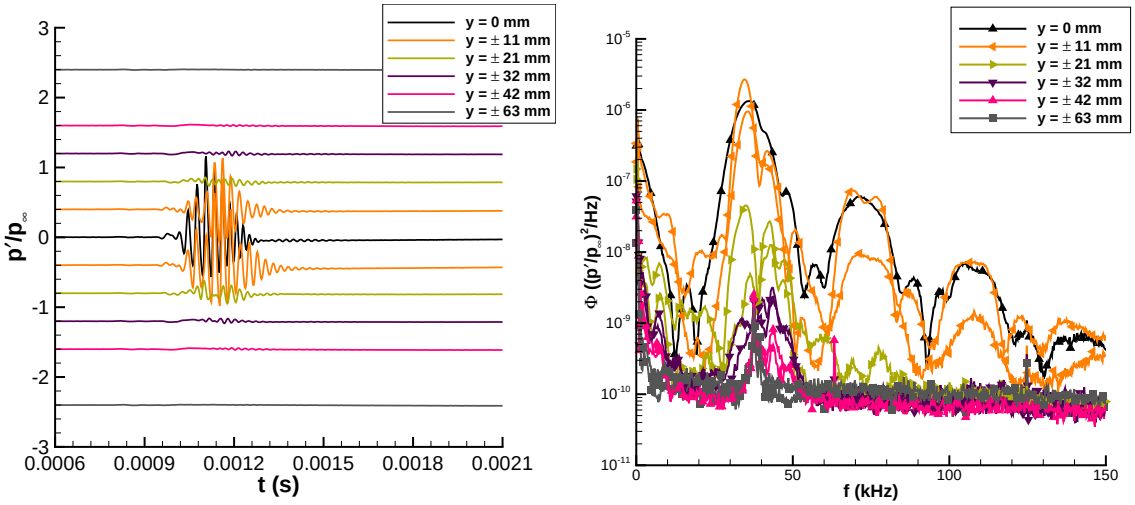

Figure 13. Spanwise measurements of ensemble-averaged disturbances at z = 2.679 m, P_0 = 836.1 kPa, T_0 = 423.8 K, $Re = 8.34 \times 10^6/m$; (a) Pressure traces, each trace is vertically offset proportional to y; (b) Power spectral density.

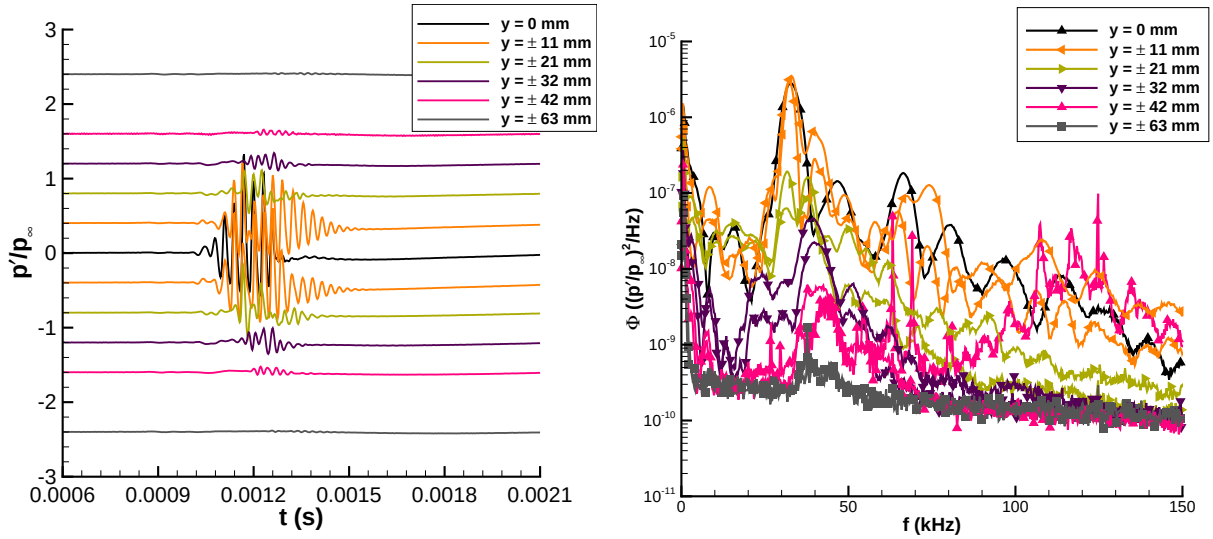

(a) (b)

Figure 14. Spanwise measurements of ensemble-averaged disturbances at z = 2.730 m, P_0 = 834.3 kPa, T_0 = 423.9 K, $Re = 8.32 \times 10^6/m$; (a) Pressure traces, each trace is vertically offset proportional to y; (b) Power spectral density.

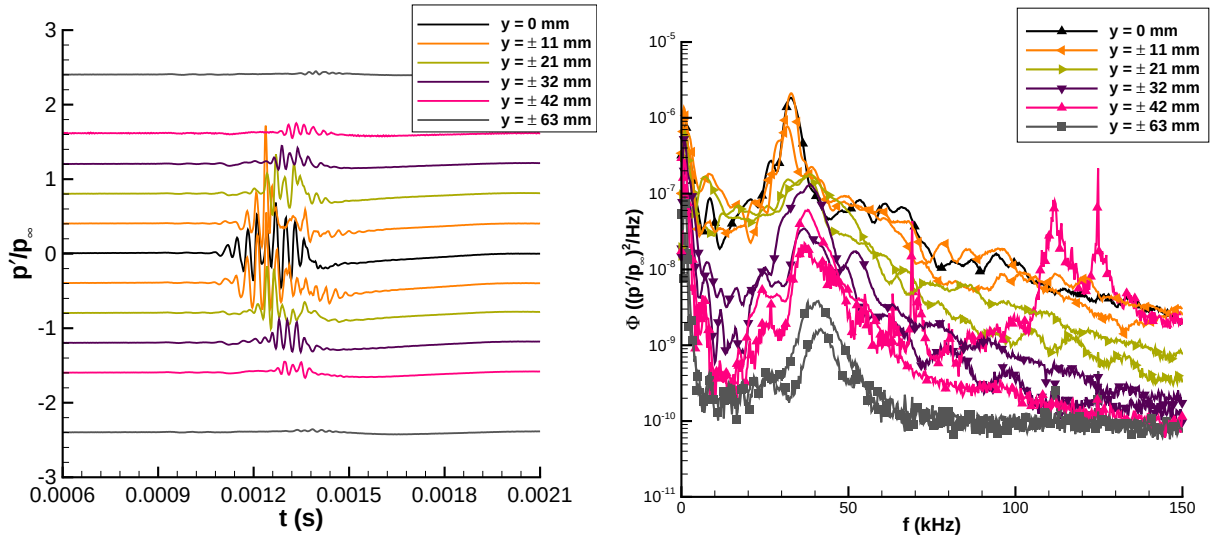

(a) (b)

Figure 15. Spanwise measurements of ensemble-averaged disturbances at z = 2.781 m, P_0 = 839.5 kPa, T_0 = 423.9 K, $Re = 8.37 \times 10^6/m$; (a) Pressure traces, each trace is vertically offset proportional to y; (b) Power spectral density.

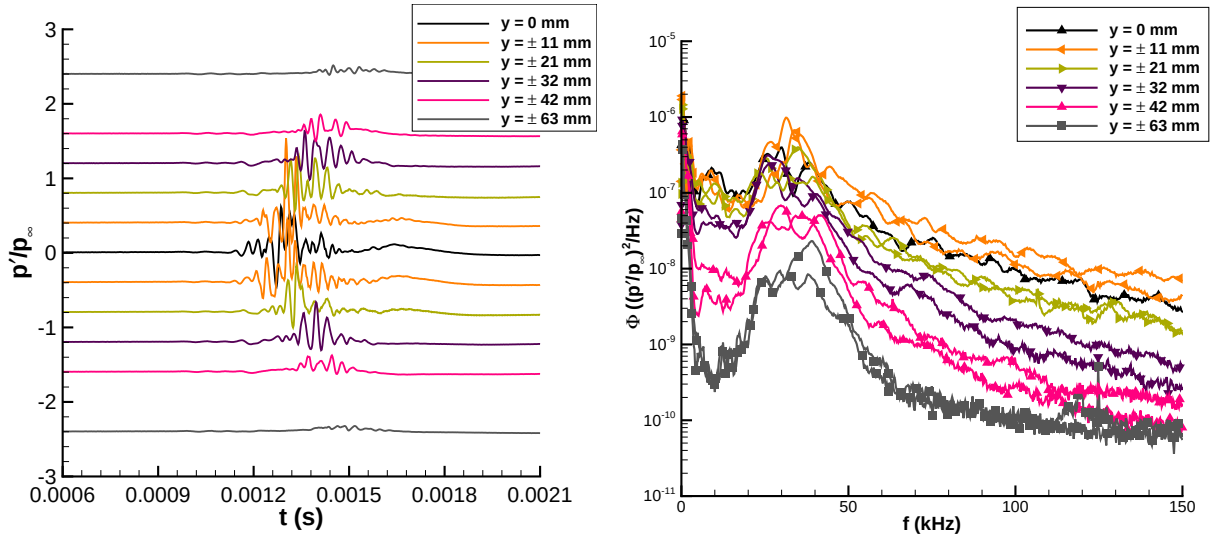

(a) (b)

Figure 16. Spanwise measurements of ensemble-averaged disturbances at z = 2.831 m, P_0 = 834.7 kPa, T_0 = 423.9 K, $Re = 8.32 \times 10^6/m$; (a) Pressure traces, each trace is vertically offset proportional to y; (b) Power spectral density.

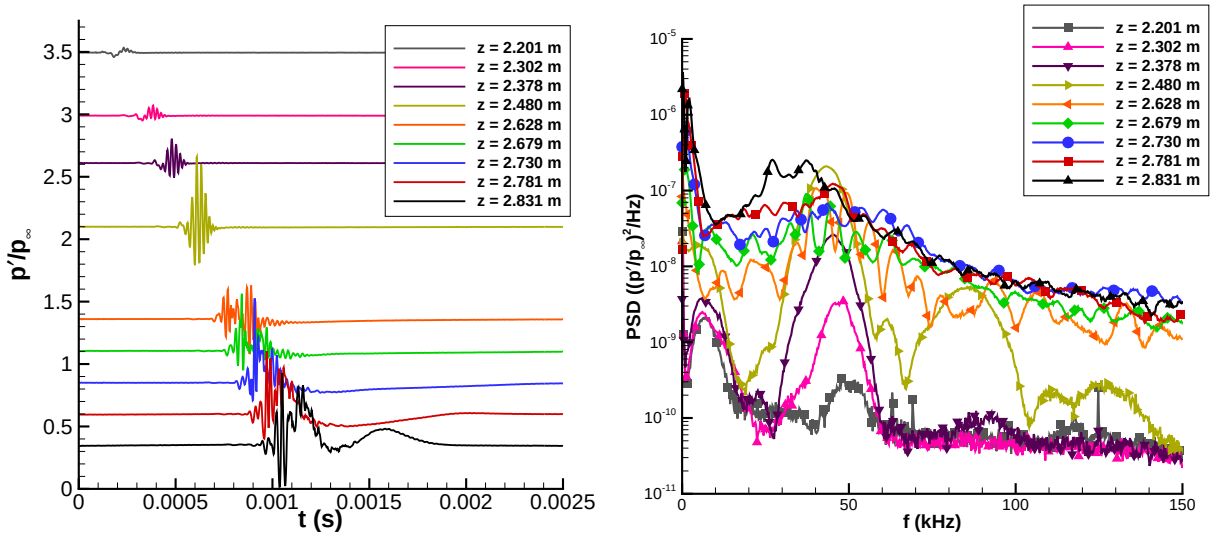

(a) (b)

Figure 17. Centerline measurements of ensemble-averaged disturbances, P_0 = 1084 kPa, T_0 = 423.8 K, $Re = 10.8 \times 10^6/m$; (a) Pressure traces, each trace is vertically offset proportional to z; (b) Power spectral density.

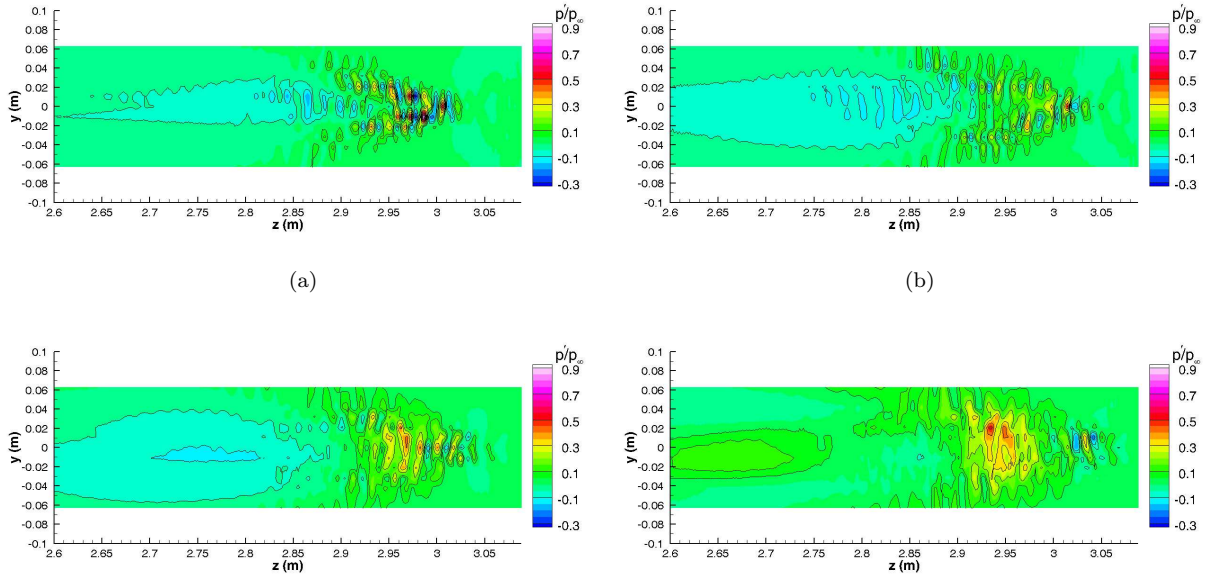

Figure 18. Contour plots of spanwise measurements of ensemble-averaged disturbances, P_0 = 1076–1088 kPa, T_0 = 423.7–424.0 K, $Re = 10.7-10.9\times10^6/m$; (a) z = 2.679 m; (b) z = 2.730 m; (c) z = 2.781 m; (d) z = 2.831 m.

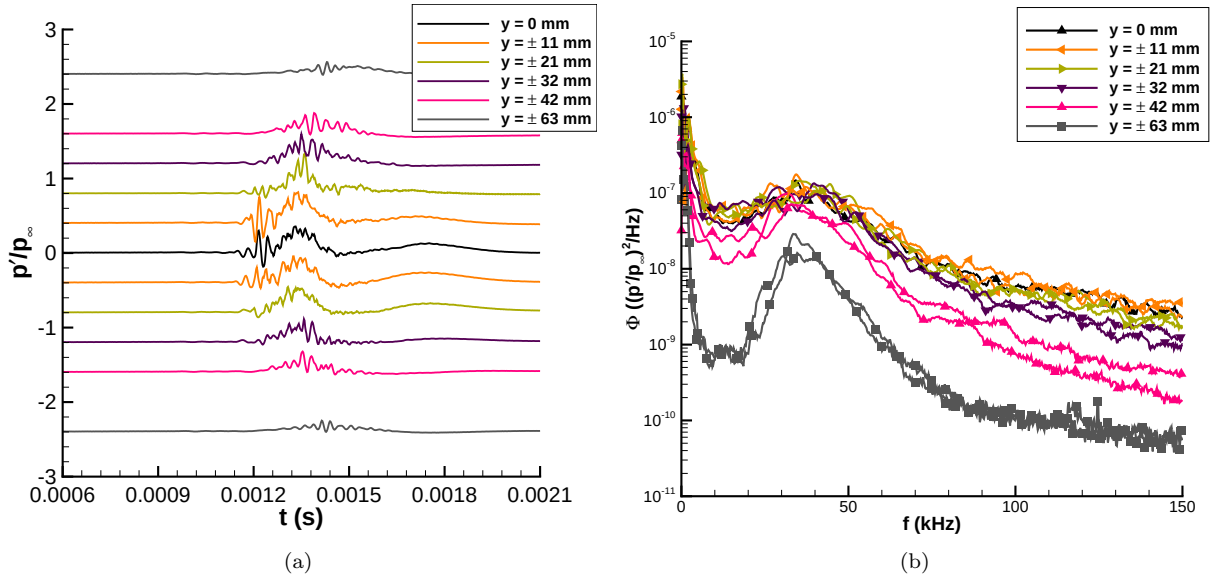

Figure 19. Spanwise measurements of ensemble-averaged disturbances at z = 2.831 m, P_0 = 1084 kPa, T_0 = 423.9 K, $Re = 10.8\times10^6/m$; (a) Pressure traces, each trace is vertically offset proportional to y; (b) Power spectral density.

IV. Concluding Remarks

Spanwise measurements have been made of pressure fluctuations beneath spark-induced disturbances. These new measurements complement the centerline data reported in Casper et al.[13] The spanwise measurements show the internal pressure structure of the disturbances during the growth and breakdown of wave packets into turbulent spots. At a low Re of $6.33 \times 10^6/m$, a small linear wave packet is formed downstream of the spark perturber. The packet grows and becomes nonlinear further downstream. At the first stages of nonlinearity, the second-mode waves are still concentrated near the centerline. As the nonlinear packet grows, it distorts and stronger waves extend in the spanwise direction. During the later stages of nonlinearity, peaks in addition to the second-mode frequency and its harmonics appear in the spectra.

At an intermediate Re of $8.25 \times 10^6/m$, the wave packet grows larger further upstream in the nozzle and eventually breaks down in the pipe insert. Once breakdown begins, stronger disturbances develop in the spanwise direction. However, even when turbulent fluctuations are seen in the core of the disturbance, second-mode waves still appear around the periphery of the turbulence. There is a gradual change in the power spectra from broadband frequency components in the core of the spot to a second-mode dominated spectra near the disturbance edges. Similar results were obtained at the highest Re of $10.8 \times 10^6/m$. In this case, breakdown of the waves occurs before the pipe insert. The resulting turbulent spot grows with downstream distance and spreads past y = $\pm$ 63 mm in the spanwise direction. At intermediate Re, there is a gradual change between the cases shown.

These measurements give a visualization of the growth and breakdown of spark-induced wave packets into turbulent spots. The spark perturbations initially generate small instability wave packets. The wave amplitudes grow with downstream distance and eventually become nonlinear, as indicated by the presence of harmonics in the spectra. The small wave packets are ordered and periodic. As they become larger, they distort and spread in the spanwise direction. During the nonlinear growth, the waves can reach large amplitudes before breaking down to turbulence. Breakdown of the waves occurs first in the middle of the packet where the amplitude of the waves is largest. After breakdown, the central region of turbulence grows downstream and the typical arrowhead shape of the spots becomes evident. However, the second-mode waves remain an integral part of the disturbance; the waves are still seen in the front and in the 'calmed' low pressure region behind the spot as well as in the spanwise edges. As the spot progresses downstream, the turbulent portion of the spot grows larger in both the streamwise and spanwise directions. The second-mode waves are evident only at the periphery of the turbulence. Because of the gradual change from a wave packet to a turbulent spot, the location when a packet becomes a spot is still unclear. These results can be used to gain a better understanding of transitional pressure fluctuations in hypersonic boundary layers and can hopefully be used towards developing a turbulent spot model of the transitional pressure fluctuations.

Acknowledgments

This work could not have been completed without the help of John Phillips, the Purdue AAE department electronics technician, who designed and built the spark perturber used for these measurements. Peter Gilbert provided the CAD model used to generate Fig. 2. Funding was provided in part by the National Science Foundation Graduate Research Fellowship Program, Sandia National Laboratories, and AFOSR.

References

[1]Laganelli, A. L., Martellucci, A., and Shaw, L. L., "Wall Pressure Fluctuations in Attached Boundary-Layer Flow," *AIAA Journal*, Vol. 21, No. 4, 1983, pp. 495–502.

[2]Pate, S. R. and Brown, M. D., "Acoustic Measurements in Supersonic Transitional Boundary Layers," AEDC-TR-69-182, October 1969.

[3]Johnson, R. I., Macourek, M. N., and Saunders, H., "Boundary Layer Acoustic Measurements in Transitional and Turbulent Flow at $M_\infty = 4.0$," AIAA Paper 69-344, April 1969.

[4]Cassanto, J. M. and Rogers, D. A., "An Experiment to Determine Nose Tip Transition with Fluctuating Pressure Measurements," *AIAA Journal*, Vol. 13, No. 10, October 1975, pp. 1257–1258.

[5]Martellucci, A., Chaump, L., Rogers, D., and Smith, D., "Experimental Determination of the Aeroacoustic Environment about a Slender Cone," *AIAA Journal*, Vol. 11, No. 5, 1973, pp. 635–642.

[6]Pate, S. R., "Dominance of Radiated Aerodynamic Noise on Boundary-Layer Transition in Supersonic/Hypersonic Wind Tunnels," AEDC-TR-77-107, March 1978.

[7]Narasimha, R., "The Laminar-Turbulent Transition Zone in the Boundary Layer," *Progress in Aerospace Sciences*, Vol. 22, January 1985, pp. 29–80.

[8]Park, S. and Lauchle, G., "Wall Pressure Fluctuation Spectra Due to Boundary-Layer Transition," *Journal of Sound and Vibration*, Vol. 319, 2009, pp. 1067–1082.

[9]Krishnan, L. and Sandham, N. D., "Effect of Mach Number on the Structure of Turbulent Spots," *Journal of Fluid Mechanics*, Vol. 566, 2006, pp. 225–234.

[10]Joksch, A. and Kleiser, L., "Growth of Turbulent Spots in High-Speed Boundary Layers on a Flat Plate," *International Journal of Heat and Fluid Flow*, Vol. 29, 2008, pp. 1543–1557.

[11]Sivasubramanian, J. and Fasel, H. F., "Direct Numerical Simulation of a Turbulent Spot in a Cone Boundary-Layer at Mach 6," AIAA Paper 2010-4599, June 2010.

[12]Sivasubramanian, J. and Fasel, H. F., "Transition Initiated by a Localized Disturbance in a Hypersonic Flat-Plate Boundary Layer," AIAA Paper 2011-374, January 2011.

[13]Casper, K., Beresh, S., and Schneider, S., "Pressure Fluctuations Beneath Turbulent Spots and Instability Wave Packets in a Hypersonic Boundary Layer," AIAA Paper 2011-372, January 2011.

[14]Keyes, F. G., "A Summary of Viscosity and Heat-Conduction Data for He, A, H_2, O_2, N_2, CO, CO_2, H_2O, and Air," *Transactions of the ASME*, Vol. 73, July 1951, pp. 589–596.

[15]Steen, L. E., *Characterization and Development of Nozzles for a Hypersonic Quiet Wind Tunnel*, Master's Thesis, Purdue University School of Aeronautics & Astronautics, December 2010.

[16]Schneider, S. P., "The Development of Hypersonic Quiet Tunnels," *Journal of Spacecraft and Rockets*, Vol. 45, No. 4, 2008, pp. 641–664.

[17]Beresh, S. J., Henfling, J. F., Spillers, R. W., and Pruett, B. O. M., "Measurements of Fluctuating Wall Pressures Beneath a Supersonic Turbulent Boundary Layer," AIAA Paper 2010-305, January 2010.

[18]Rotea, M. A., Randall, L. A., Song, G., and Schneider, S. P., "Model Identification of a Kulite Pressure Transducer," AIAA Paper 96-2278, June 1996.

[19]Juliano, T., Segura, R., Borg, M., Casper, K., Hannon, M., Wheaton, B., and Schneider, S., "Starting Issues and Forward-Facing Cavity Resonance in a Hypersonic Quiet Tunnel," AIAA Paper 2008-3730, June 2008.

[20]Watmuff, J. H., "Detrimental Effects of Almost Immeasurably Small Freestream Nonuniformities Generated by Wind-Tunnel Screens," *AIAA Journal*, Vol. 36, No. 3, March 1998, pp. 379–386.

[21]Kimmel, R. L., Demetriades, A., and Donaldson, J. C., "Space-Time Correlation Measurements in a Hypersonic Transitional Boundary Layer," AIAA Paper 95-2292, June 1995.